

Microtubule Tracking in Electron Microscopy Volumes

Nils Eckstein^{1,2,*}, Julia Buhmann^{1,2}, Matthew Cook², Jan Funke¹

¹HHMI Janelia Research Campus, Ashburn, USA,

²Institute of Neuroinformatics UZH/ETHZ, Zurich, Switzerland,

*Corresponding author: ecksteinn@janelia.hhmi.org

Abstract. We present a method for microtubule tracking in electron microscopy volumes. Our method first identifies a sparse set of voxels that likely belong to microtubules. Similar to prior work, we then enumerate potential edges between these voxels, which we represent in a candidate graph. Tracks of microtubules are found by selecting nodes and edges in the candidate graph by solving a constrained optimization problem incorporating biological priors on microtubule structure. For this, we present a novel integer linear programming formulation, which results in speed-ups of three orders of magnitude and an increase of 53% in accuracy compared to prior art (evaluated on three $1.2 \times 4 \times 4\mu m$ volumes of *Drosophila* neural tissue). We also propose a scheme to solve the optimization problem in a block-wise fashion, which allows distributed tracking and is necessary to process very large electron microscopy volumes. Finally, we release a benchmark dataset for microtubule tracking, here used for training, testing and validation, consisting of eight $30 \times 1000 \times 1000$ voxel blocks ($1.2 \times 4 \times 4\mu m$) of densely annotated microtubules in the CREMI data set (<https://github.com/nilsec/micron>).

1 Introduction

Microtubules are part of the cytoskeleton of a cell and crucial for a variety of cellular processes such as structural integrity and intracellular transport of cargo [15]. They are of particular interest for the connectomics community, as they directly follow the morphology of neurons. Tracking of microtubules therefore provides additional structural information that can potentially be leveraged for guided proof-reading of neuron segmentation and aid in the identification of neural subcompartments such as backbones and twigs [17].

Manual tracking of microtubules faces the same limitations as neuron segmentation and synapse annotations. The resolution needed to discern individual structures of interest like neural arbors, synapses, and microtubules can only be achieved with high resolution electron microscopy (EM), which results in large datasets (several hundred terabytes) even for small model organisms like *Drosophila melanogaster* [22]. With datasets of these sizes, a purely manual analysis becomes impractical. Consequently, the field of connectomics sparked a surge of automatic methods to segment neurons (for recent advances see [7, 11, 13, 14]),

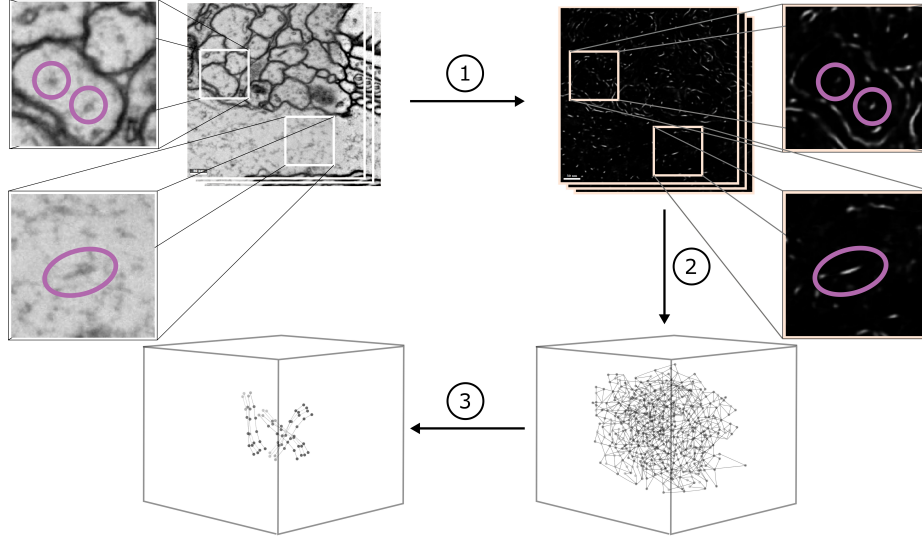


Fig. 1: Overview of the proposed method. **1.** Microtubule scores are predicted via a 3D UNet [16]. Inlets show two microtubules that run perpendicular to the imaging plane (appearing as circles) and one that deviates from a 90 degree angle of incidence (appearing as a line segment). The corresponding (noisy) microtubule scores show the necessity of post processing. **2.** Candidate microtubule segments are extracted and represented as vertices in a 3D graph, where vertices are connected within a threshold distance. **3.** Final microtubule trajectories are found by solving a constrained optimization problem.

annotate synapses [2, 3, 6, 9, 10, 12, 19], and identify other structures of biological relevance such as microtubules [4] or mitochondria [5, 6, 21]. Large scale automatic reconstruction of microtubules is a particularly challenging problem. With an outer diameter of 24 nm , microtubules are close to the resolution limit of serial section EM¹. Especially in anisotropic EM volumes, the appearance of microtubules changes drastically depending on their angle of incidence to the imaging plane. Furthermore, they are often locally indistinguishable from other cell organelles (like endoplasmic reticulum) or noise.

Our method for microtubule tracking is based on the formulation proposed in [4], with significant improvements in terms of efficiency and accuracy. Similar to [4], we first predict a score for each voxel to be part of a microtubule. We then identify promising candidate points and possible links between them in a candidate graph as nodes and edges. Finally, we solve a constraint optimization

¹ Resolution is around $4 \times 4 \times 40\text{ nm}$ for ssTEM, and $8 \times 8 \times 8\text{ nm}$ for FIB-SEM [20].

problem incorporating biological priors to find a subset of edges that constitute microtubule tracks (for an overview see Fig. 1).

Our four main contributions are as follows: 1. We propose a new integer linear program (ILP) formulation, which decreases the time needed to solve the constraint optimization by several orders of magnitude. 2. We devise a scheme to solve the resulting optimization problem in a block-wise fashion in linear time, and thus are able to process real-world sized volumes. 3. Our formulation allows tracking of microtubules in arbitrary orientations in anisotropic volumes by introducing a non-maxima suppression (NMS) based candidate extraction method. 4. We improve the voxel-level classifier by training a 3D UNet [7, 16] on skeleton annotations, leading to more accurate microtubule scores.

We evaluate our method on a new benchmark comprising $153.6 \mu\text{m}^3$ of densely traced microtubules, demonstrating a 53% increase in accuracy ($0.517 \rightarrow 0.789$ F1 score) compared to the prior state of the art. Source code and datasets are publicly available at <https://github.com/nilsec/micron>.

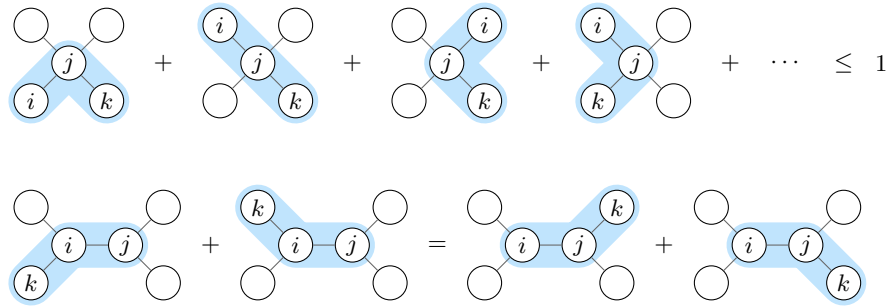
2 Method

2.1 Predictions

Starting from the raw EM input data, we train a 3D UNet [16] to predict a microtubule score $m \in [0, 1]$ for each voxel. We generate microtubule scores for training from manually annotated skeletons by interpolating between skeleton markers on a voxel grid followed by Gaussian smoothing. In addition, we train the network to predict spatial gradients of the microtubule score up to second order. This is motivated by the idea that the spatial gradient encodes the local shape of a predicted object. Since microtubule segments have locally line-like shapes this auxiliary task potentially regularises microtubule score predictions.

2.2 Candidate Extraction

Given the predicted microtubule score we perform candidate extraction via two NMS passes, to guarantee that two successive candidates of a single microtubule track are not farther apart than the distance threshold θ_d we will use to connect two candidates with each other. In a first pass, we perform NMS and thresholding with a stride equal to the NMS window size, guaranteeing at least one candidate per NMS window if the maximum is above the threshold. This strategy is problematic if the local maximum lies on the boarder or corner of a NMS window as this produces multiple, in the worst case eight, candidates that are direct neighbors of each other. We remove this redundancy by performing a second NMS pass on the already extracted maxima, providing us with the final set of microtubule segment candidate detections C .



(a) Consistency constraints (top row) and no-branch constraints (bottom row).

$\begin{aligned} \min_{I_{i,j,k}} \quad & \sum_{i \in V} c_i \cdot I_i + \sum_{(i,j) \in E} c_{i,j} \cdot I_{i,j} + \sum_{(i,j,k) \in T} c_{i,j,k} \cdot I_{i,j,k} \\ \text{s.t.} \quad & \\ \forall (i,j,k) \in T: \quad & I_i, I_{i,j}, I_{i,j,k} \in \{0,1\} \\ \forall i \in V: \quad & 2I_i - \sum_{(i,j) \in E} I_{i,j} = 0 \\ \forall (i,j) \in E: \quad & 2I_{i,j} - I_i - I_j \leq 0 \\ \forall (i,j,k) \in T: \quad & 2I_{i,j,k} - I_{i,j} - I_{j,k} \leq 0 \\ & -I_{i,j,k} + I_{i,j} + I_{j,k} \leq 1 \end{aligned}$	$\begin{aligned} \min_{I_{i,j,k}} \quad & \sum_{(i,j,k) \in T} c_{i,j,k} \cdot I_{i,j,k} \\ \text{s.t.} \quad & \\ \forall (i,j,k) \in T: \quad & I_{i,j,k} \in \{0,1\} \\ \forall j \in V: \quad & \sum_{(i,j,k) \in T} I_{i,j,k} \leq 1 \\ \forall (i,j) \in E: \quad & \sum_{(k,i,j) \in T} I_{k,i,j} - \sum_{(i,j,k) \in T} I_{i,j,k} = 0 \end{aligned}$
---	--

(b) ILP following [4].

(c) Reformulated ILP on triplet indicators.

Fig. 2: Constraint optimization on the candidate graph. We formulate an ILP on binary triplet indicators, which encode the joint selection of two incident candidate edges. The constraints shown in (a) ensure that found tracks are not crossing or splitting. Although mathematically equivalent to the formulation in (b), our formulation (c) is orders of magnitudes more efficient (see Fig. 4).

2.3 Constrained Optimization

Following [4], we represent each candidate microtubule segment $i \in C$ as a node in a graph with an associated position $p_i = (x_i, y_i, z_i)$. A priori we do not know which microtubule segments $i \in C$ belong together and form a microtubule. Thus, we connect all microtubule candidates with each other that are below a certain distance threshold θ_d . More formally, we introduce an undirected graph $G = (V, E)$, where $V = C \cup \{S\}$ is the set of microtubule candidate segments C augmented with a special node S and $E \subset V \times V$ is the set of possible links between them. The special node S is used to mark the beginning or end of a microtubule track and is connected to all candidates in C . We further define a set $T = \{(i, j, k) \in V \times C \times V \mid (i, j), (j, k) \in E, i \neq k\}$ of all directly connected triplets on G .

As observed in [4], we can make use of the fact that microtubules do not branch and have limited curvature [8]. We encode these priors as constraints and costs respectively, and solve the resulting optimization problem with an ILP. As outlined in Fig. 2, and in contrast to [4], we formulate consistency and

”no-branch” constraints on triplets of connected nodes $(i, j, k) \in T$ only, leading to an orders of magnitude improvement in ILP solve time (see Fig. 4). To this end, we introduce a binary indicator variable $I_{i,j,k} \in \{0, 1\}$ for each $(i, j, k) \in T$ and define selection costs $c_{i,j,k}$ for each triplet by propagating costs c_i on nodes and $c_{i,j}$ on edges as follows:

$$c_i = \begin{cases} \theta_S & \text{if } i = S \\ \theta_P & \text{else} \end{cases} \quad \begin{cases} c_{i,j} = \theta_D \text{dist}(i, j) + \theta_E \text{evid}(i, j) + c_i + c_j \\ c_{i,j,k} = \theta_C \text{curv}(i, j, k) + c_{i,j} + c_{j,k} \end{cases}, \quad (1)$$

where θ_S is the cost for beginning/ending a track and $\theta_P < 0$ is the prior on node selection. $\text{dist}(i, j) = \|p_i - p_j\|$ measures the distance between candidates i and j , whereas $\text{evid}(i, j) = \sum_{p \in P_{i,j}} m(p)$ accumulates the predicted evidence for microtubules on all voxels on a line $P_{i,j}$ connecting i and j . $\text{curv}(i, j, k) = \pi - \angle(i, j, k)$ measures deviations of a 180 degree angle between two pairs of edges, and thus introduces a cost on curvature. The values $\theta_S, \theta_P, \theta_D, \theta_E, \theta_C \in \mathbb{R}$ are free parameters of the method and found via grid search on a validation dataset.

2.4 Blockwise Processing

In order to be able to apply the constraint optimization to arbitrary sized volumes, we decompose the candidate graph spatially into a set of blocks B . For each block $b \in B$, we define a constant-size context region \bar{b} , which encloses the block and is chosen to be large enough such that decisions outside the context region are unlikely to change the ILP solution inside the block. We next identify sets $S_i \subset B$ of blocks that are pairwise conflict free, where we define two blocks a and b to be in conflict if a overlaps with \bar{b} . All blocks of a subset S_i can then be distributed and processed in parallel. The corresponding ILP for each block $b \in S_i$ is solved within \bar{b} , however, assignments of the binary indicators are only stored for indicators corresponding to nodes in b . To obtain consistent solutions across block boundaries, existing indicator assignments from previous runs of conflicting blocks are acknowledged by adding additional constraints to the block ILP. See supplement for an illustration.

2.5 Evaluation

To evaluate reconstructed tracks against groundtruth, we resample both reconstruction and groundtruth tracks equidistantly and match nodes based on distance using Hungarian matching. Results are reported in terms of precision and recall on edges, which we consider correct if they connect two matched nodes that are matched to the same track.

3 Results

3.1 Dataset

We densely annotated microtubules in eight $1.2 \times 4 \times 4 \mu\text{m}$ ($30 \times 1000 \times 1000$ voxel) volumes of EM data in all six CREMI² volumes A, B, C, A+, B+, C+ using

² MICCAI Challenge on Circuit Reconstruction in EM Images, <https://cremi.org>.

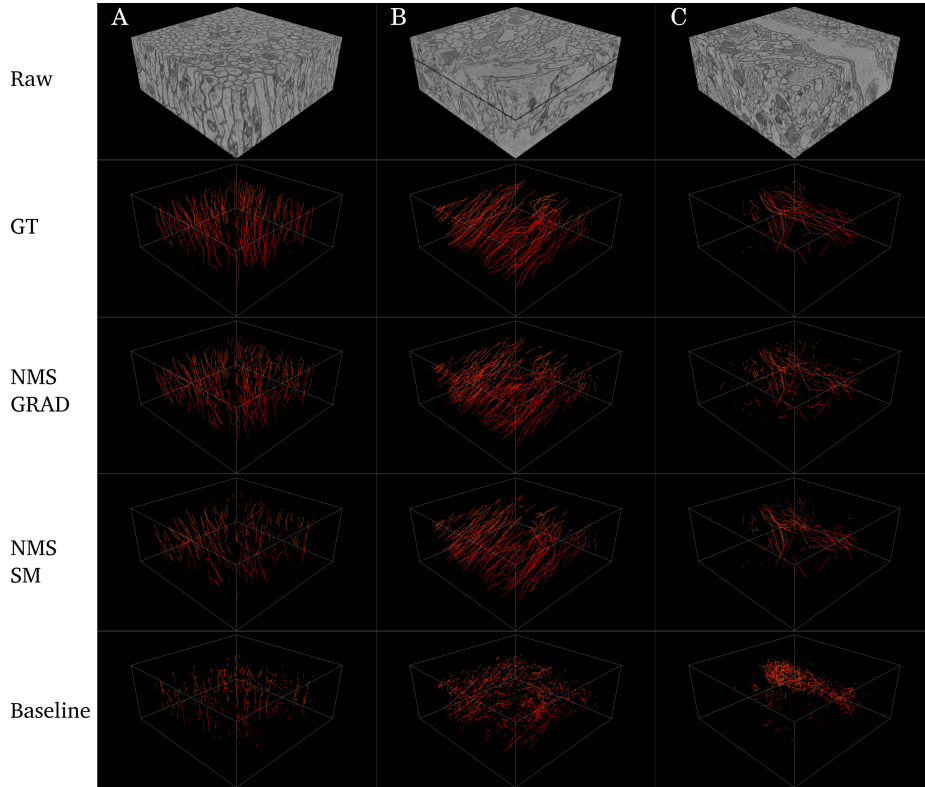


Fig. 3: 3D rendering of raw EM volumes (Raw), manual tracing (GT) and automatically reconstructed microtubules in CREMI volumes A,B,C for our method (NMS_GRAD and NMS_SM) and the considered baseline [4] using validation best ILP parameters (best viewed on screen).

Knossos [1] and split the data in training (A+, B+, C+), validation (B+v, B_v) and test (A, B, C) sets.

3.2 Comparison

*NMS_** models refer to the model described in the methods section, where NMS_SM uses a 3D UNet predicting microtubule score only, NMS_GRAD additionally predicts spatial gradients of the microtubule score up to second order and NMS_RFC uses a random forest classifier (RFC) instead of a 3D UNet. For each, we first select the best performing UNet architecture (for NMS_RFC we interactively train an RFC using Ilastik [18]) and NMS candidate extraction threshold in terms of recovered candidates on the validation datasets, followed by a grid search over the distance threshold θ_d and ILP parameters for 150 different parameter combinations. For the NMS candidate extraction we use a window size of 1x10x10 voxels for the first NMS pass to offset the anisotropic resolution of 40x4x4 nm. For the second NMS pass we use a window size of 1x3x3 voxels,

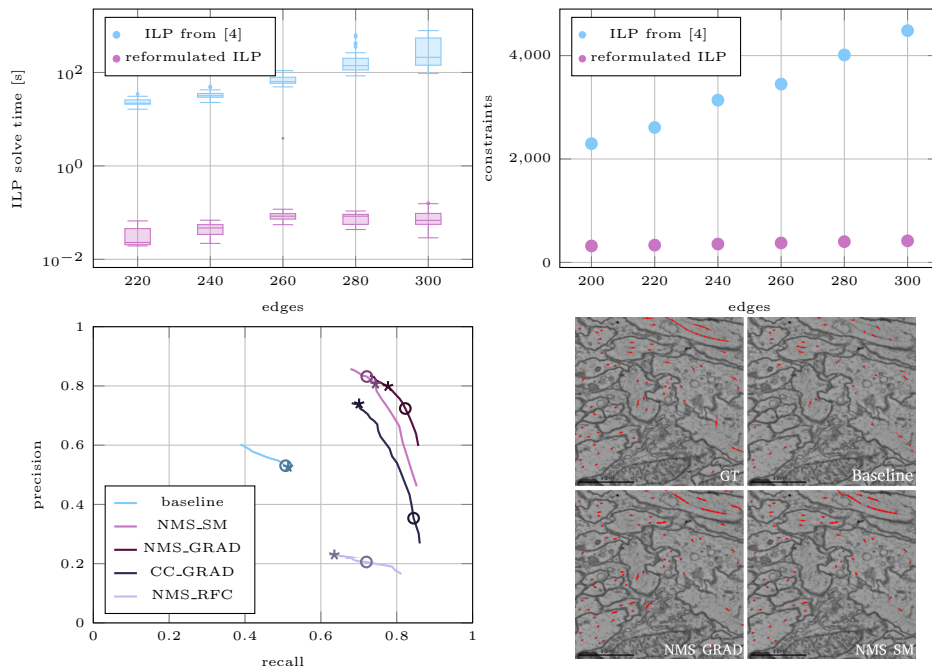


Fig. 4: **Top row:** comparison of ILP formulations on random candidate graphs in terms of solve time (left) and number of constraints (right). Solve times have been obtained from 54 different ILP parameter configurations $\theta_{S,P,D,E,C}$ on an Intel Xeon(R), 2.40GHz x 16 CPU processor using the Gurobi optimizer. **Bottom row, left:** Comparison of our method (NMS_SM and NMS_GRAD) to the baseline [4] and two ablation experiments CC_GRAD (NMS replaced with connected component candidate extraction) and NMS_RFC (UNet replaced with RFC). Shown are precision and recall for varying values of the start/end edge prior θ_S averaged over the test datasets A,B,C. The validation and test best are highlighted with circles and stars, respectively. **Bottom row, right:** Qualitative results on sample B (best viewed on screen).

removing double detections.

Baseline refers to an adaptation³ of the method in [4], that uses an RFC for prediction, z section-wise connected component (CC) analysis on the thresholded microtubule scores for candidate extraction, and a fixed orientation estimate for each microtubule candidate pointing in the z direction⁴. For the baseline we interactively train two (for microtubules of different angles of incidence on the imaging plane) RFCs on training volumes A, B, C using Ilastik [18]. We find the threshold for CC candidate extraction, distance threshold θ_d and ILP parame-

³ We use our ILP formulation, which was necessary to process larger volumes.

⁴ Orientation estimate used in [4] (direct communication with authors).

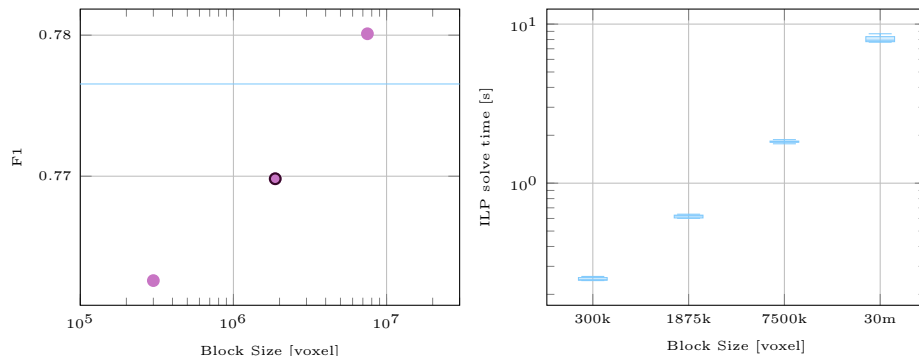


Fig. 5: **Left:** Accuracy as a function of block size over several orders of magnitude. Shown are the F1 scores, averaged over test data sets A, B and C, using validation best parameters NMS_GRAD. Interestingly, for some sizes, solving the ILP block-wise results in higher F1 scores than solving the ILP to global optimality (blue line). However, it should be noted that the differences in F1 score are minor and likely not significant. The black circle indicates the block size we used for all reported results. **Right:** Box plot of ILP solve time per block as a function of block size. Shown is the wall-clock time needed to solve the ILP for one block, measured for ten runs, on test cube B using validation best parameters NMS_GRAD. Note that in contrast to accuracy, solve time is strongly affected by block size. This implies that we are able to process large volumes by solving the ILP in a blockwise manner, without a significant decrease in accuracy.

ters via grid search over 242 parameter configurations on the validation set. For an overview see Table 1.

3.3 Test Results

Fig. 4 shows that both variants of our proposed model outperform the prior state of the art [4] substantially. Averaged over test data sets A,B,C, we demonstrate a 53% increase in accuracy for NMS_GRAD. Table 1 further shows test best F1 scores for each individual dataset. In accordance with the qualitative results shown in Fig. 3, NMS_GRAD performs substantially better for test set A while NMS_SM is more accurate for volumes B and C. Ablation experiments show that CC candidate extraction leads to overall less accurate reconstructions. Exchanging the UNet with an RFC while retaining NMS candidate extraction seriously harms performance, resulting in large numbers of false positive detections. For extended qualitative results, including reconstruction of microtubules in the Calyx, a $76 \times 52 \times 64 \mu\text{m}$ region of the *Drosophila Melanogaster* brain, see supplement.

Table 1: Model overview and test best F1 score by data set.

Model	Prediction	Cand. Extr.	Edge Score	A	B	C	Avg
NMS_GRAD	UNet+GRAD	NMS	Evidence	0.784	0.827	0.757	0.789
NMS_SM	UNet	NMS	Evidence	0.711	0.828	0.785	0.775
Baseline	RFC	CC	Orientation	0.454	0.547	0.549	0.517
CC_GRAD	UNet+GRAD	CC	Evidence	0.660	0.723	0.537	0.640
NMS_RFC	RFC	NMS	Evidence	0.366	0.375	0.302	0.348

4 Discussion

Although some of our improvements in accuracy can be attributed to the use of a deep learning classifier, the presented method relies mostly on an effective way of incorporating biological priors in the form of constraint optimization. In particular our ablation studies (CC_GRAD) show that the strided NMS-based candidate extraction method positively impacts accuracy: Since a single microtubule could potentially extend far in the x-y imaging plane, it is not sufficient to represent candidates in one plane by a single node, as done in [4]. The strided NMS detections homogenize the candidate graph and likely allow transferring our method to datasets of different resolutions. A potential downside is poor precision when combined with extremely noisy microtubule score predictions m (see NMS_RFC). In this case NMS on a grid extracts too many candidate segments, and besides structural priors, the only remaining cost we use to extract final microtubule tracks is directly derived from the (noisy) predicted microtubule score m (see equation (1)). Note that the baseline does not suffer as much from noisy microtubule scores, because it uses a fixed orientation prior and is thus limited to a subset of microtubules in any given volume. Finally, the reformulation of the ILP and the block-wise processing scheme result in a dramatic speed-up and the ability to perform distributed, consistent tracking, which is required to process petabyte-sized datasets.

5 Acknowledgements

We thank Tri Nguyen and Caroline Malin-Mayor for code contribution; Arlo Sheridan for helpful discussions and Albert Cardona for his contagious enthusiasm and support. This work was supported by Howard Hughes Medical Institute and Swiss National Science Foundation (SNF grant 205321L 160133).

References

1. Boergens, K.M., Berning, M., Bocklisch, T., Bräunlein, D., Drawitsch, F., Frohn-hofen, J., Herold, T., Otto, P., Rzepka, N., Werkmeister, T., et al.: webknossos: efficient online 3d data annotation for connectomics. *nature methods* **14**(7), 691–694 (2017)

2. Buhmann, J., Krause, R., Ceballos Lentini, R., Eckstein, N., Cook, M., Turaga, S., Funke, J.: Synaptic partner prediction from point annotations in insect brains. *Medical Image Computing and Computer Assisted Intervention MICCAI 2018* **11071** (09 2018)
3. Buhmann, J., Sheridan, A., Gerhard, S., Krause, R., Nguyen, T., Heinrich, L., Schlegel, P., Lee, W.C.A., Wilson, R., Saalfeld, S., Jefferis, G., Bock, D., Turaga, S., Cook, M., Funke, J.: Automatic detection of synaptic partners in a whole-brain drosophila em dataset. *bioRxiv* (2019). <https://doi.org/10.1101/2019.12.12.874172>, <https://www.biorxiv.org/content/early/2019/12/13/2019.12.12.874172>
4. Buhmann, J.M., Gerhard, S., Cook, M., Funke, J.: Tracking of microtubules in anisotropic volumes of neural tissue. In: *2016 IEEE 13th International Symposium on Biomedical Imaging (ISBI)* (2016). <https://doi.org/10.1109/isbi.2016.7493275>, <http://dx.doi.org/10.1109/ISBI.2016.7493275>
5. Cheng, H.C., Varshney, A.: Volume segmentation using convolutional neural networks with limited training data. In: *2017 IEEE international conference on image processing (ICIP)*. pp. 590–594. IEEE (2017)
6. Dorkenwald, S., Schubert, P.J., Killinger, M.F., Urban, G., Mikula, S., Svava, F., Kornfeld, J.: Automated synaptic connectivity inference for volume electron microscopy. *Nature methods* **14**(4), 435–442 (2017)
7. Funke, J., Tschopp, F.D., Grisaitis, W., Sheridan, A., Singh, C., Saalfeld, S., Turaga, S.C.: Large scale image segmentation with structured loss based deep learning for connectome reconstruction. *IEEE Transactions on Pattern Analysis and Machine Intelligence* pp. 1–1 (2018). <https://doi.org/10.1109/TPAMI.2018.2835450>
8. Gittes, F., Mickey, B., Nettleton, J., Howard, J.: Flexural rigidity of microtubules and actin filaments measured from thermal fluctuations in shape. *The Journal of cell biology* **120**(4), 923–934 (1993)
9. Heinrich, L., Funke, J., Pape, C., Nunez-Iglesias, J., Saalfeld, S.: Synaptic cleft segmentation in non-isotropic volume electron microscopy of the complete drosophila brain. In: *International Conference on Medical Image Computing and Computer-Assisted Intervention*. pp. 317–325. Springer (2018)
10. Huang, G.B., Scheffer, L.K., Plaza, S.M.: Fully-automatic synapse prediction and validation on a large data set. *Frontiers in neural circuits* **12**, 87 (2018)
11. Januszewski, M., Kornfeld, J., Li, P.H., Pope, A., Blakely, T., Lindsey, L., Maitin-Shepard, J., Tyka, M., Denk, W., Jain, V.: High-precision automated reconstruction of neurons with flood-filling networks. *Nature methods* p. 1 (2018)
12. Kreshuk, A., Funke, J., Cardona, A., Hamprecht, F.A.: Who is talking to whom: Synaptic partner detection in anisotropic volumes of insect brain. In: Navab, N., Hornegger, J., Wells, W.M., Frangi, A. (eds.) *Medical Image Computing and Computer-Assisted Intervention – MICCAI 2015*. pp. 661–668. Springer International Publishing, Cham (2015)
13. Lee, K., Lu, R., Luther, K., Seung, H.S.: Learning Dense Voxel Embeddings for 3D Neuron Reconstruction. *arXiv e-prints arXiv:1909.09872* (Sep 2019)
14. Lee, K., Zung, J., Li, P., Jain, V., Seung, H.S.: Superhuman accuracy on the snemi3d connectomics challenge. *arXiv preprint arXiv:1706.00120* (2017)
15. Nogales, E.: Structural insights into microtubule function. *Annual Review of Biochemistry* **69**(1), 277–302 (2000)
16. Ronneberger, O., Fischer, P., Brox, T.: U-net: Convolutional networks for biomedical image segmentation. In: *International Conference on Medical image computing and computer-assisted intervention*. pp. 234–241. Springer (2015)

17. Schneider-Mizell, C.M., Gerhard, S., Longair, M., Kazimiers, T., Li, F., Zwart, M.F., Champion, A., Midgley, F.M., Fetter, R.D., Saalfeld, S., et al.: Quantitative neuroanatomy for connectomics in drosophila. *eLife* **5**, e12059 (2016)
18. Sommer, C., Straehle, C.N., Koethe, U., Hamprecht, F.A., et al.: Ilastik: Interactive learning and segmentation toolkit. In: ISBI. vol. 2, p. 8 (2011)
19. Staffler, B., Berning, M., Boergens, K.M., Gour, A., van der Smagt, P., Helmstaedter, M.: Synem, automated synapse detection for connectomics. *Elife* **6**, e26414 (2017)
20. Takemura, S.y., Xu, C.S., Lu, Z., Rivlin, P.K., Parag, T., Olbris, D.J., Plaza, S., Zhao, T., Katz, W.T., Umayam, L., et al.: Synaptic circuits and their variations within different columns in the visual system of drosophila. *Proceedings of the National Academy of Sciences* **112**(44), 13711–13716 (2015)
21. Xiao, C., Chen, X., Li, W., Li, L., Wang, L., Xie, Q., Han, H.: Automatic mitochondria segmentation for em data using a 3d supervised convolutional network. *Frontiers in Neuroanatomy* **12**, 92 (2018). <https://doi.org/10.3389/fnana.2018.00092>, <https://www.frontiersin.org/article/10.3389/fnana.2018.00092>
22. Zheng, Z., Lauritzen, J.S., Perlman, E., Robinson, C.G., Nichols, M., Milkie, D., Torrens, O., Price, J., Fisher, C.B., Sharifi, N., et al.: A complete electron microscopy volume of the brain of adult drosophila melanogaster. *Cell* **174**(3), 730–743 (2018)